# Supporting Information

**Bifunctional electrocatalyst based on interfacial engineering of $CeO_2$ and $NiSe_2$ for boosting electrocatalytic water splitting**

Xueying Wang,[#a] Yunong Qin,[#a] Xin Peng,[a] Ling Li,*[a] Qiancheng Zhu,[a] and Wenming Zhang*[a]

[a] *Province-Ministry Co-construction Collaborative Innovation Center of Hebei Photovoltaic Technology, College of Physics Science and Technology, Hebei University, Baoding 071002, China.*

**Corresponding author:**

E-mail: lilinghbu@163.com (L. Li), wmzhang@hbu.edu.cn (W. Zhang)

**List of Contents**

## 1. Computational Simulation Process

We have employed the first-principles[1,2] to perform all density functional theory (DFT) calculations within the generalized gradient approximation (GGA) using the Perdew-Burke-Ernzerhof (PBE)[3] formulation. We have chosen the projected augmented wave (PAW) potentials[4,5] to describe the ionic cores and take valence electrons into account using a plane wave basis set with a kinetic energy cutoff of 520 eV. Partial occupancies of the Kohn−Sham orbitals were allowed using the Gaussian smearing method with a width of 0.05 eV. The electronic energy was considered self-consistent when the energy change was smaller than $10^{-4}$ eV. A geometry optimization was considered convergent when the energy change was smaller than 0.05 eV $Å^{-1}$. The vacuum spacing in a direction perpendicular to the plane of the structure is 20 Å for the surfaces. The Brillouin zone integration is performed using 2×2×1 Monkhorst-Pack k-point sampling for a structure. Finally, the adsorption energies (Eads) were calculated as Eads= Ead/sub -Ead -Esub, where Ead/sub, Ead, and Esub are the total energies of the optimized adsorbate/substrate system, the adsorbate in the structure, and the clean substrate, respectively. The free energy was calculated using the equation:

$$G = Eads + ZPE - TS \quad (1)$$

where G, Eads, ZPE and TS are the free energy, total energy from DFT calculations, zero point energy and entropic contributions, respectively.

## 2. Supplementary Figures

**Figure S1.** EDX plot of $CeO_2$-$NiSe_2$.

**Figure S2.** SEM images of (a) $CeO_2$-$NiSe_2$-500, (b) $CeO_2$-$NiSe_2$-1200, (c) $CeO_2$-$NiSe_2$-2400.

**Figure S3.** XPS spectrum of the $CeO_2$-$NiSe_2$ and $NiSe_2$. (a) Ni 2p, (b) Ce 3d.

**Figure S4.** (a) Ni 2p and (b) Ce 3d XPS spectrum of the $CeO_2$-$NiSe_2$ and $NiSe_2$ after OER stability test.

**Figure S5.** Chronopotentiometry measurements on the long-term stability of the $CeO_2$-$NiSe_2$ during (a) OER and (b) HER electrolysis.

**Figure S6.** (a)-(c) SEM images of $CeO_2$-$NiSe_2$ after OER stability test.

**Figure S7.** (a)-(c) TEM images of $CeO_2$-$NiSe_2$ after OER stability test.

**Figure S8.** HRTEM images of $CeO_2$-$NiSe_2$ after OER stability test.

**Figure S9.** XRD pattern of $CeO_2$-$NiSe_2$ before and after OER stability test.

**Figure S10.** Raman spectrum of $CeO_2$-$NiSe_2$ before and after OER stability test.

**Figure S11.** CVs of OER measurements in 1 M KOH at scan rates from 20 to 80 mV $s^{-1}$ for (a) $CeO_2$-$NiSe_2$, (b) $Ni(OH)_2$, (c) $NiSe_2$ and (d) $CeO_2$.

**Figure S12.** OER performance of $CeO_2$-$NiSe_2$ at different deposition time. (a) LSV curves of $CeO_2$-$NiSe_2$-500, $CeO_2$-$NiSe_2$-1200, $CeO_2$-$NiSe_2$-2400. (b) Tafel plots of $CeO_2$-$NiSe_2$-500, $CeO_2$-$NiSe_2$-1200, $CeO_2$-$NiSe_2$-2400. (c) Nyquist plots derived from EIS measurements of $CeO_2$-$NiSe_2$-500, $CeO_2$-$NiSe_2$-1200, $CeO_2$-$NiSe_2$-2400.

**Figure S13.** CVs of HER measurements in 1 M KOH at scan rates from 20 to 80 mV $s^{-1}$ for (a) $CeO_2$-$NiSe_2$, (b) $Ni(OH)_2$, (c) $NiSe_2$ and (d) $CeO_2$.

**Figure S14.** HER performance of $CeO_2$-$NiSe_2$ at different deposition time. (a) LSV curves of $CeO_2$-$NiSe_2$-500, $CeO_2$-$NiSe_2$-1200, $CeO_2$-$NiSe_2$-2400. (b) Tafel plots of

$CeO_2$-$NiSe_2$-500, $CeO_2$-$NiSe_2$-1200, $CeO_2$-$NiSe_2$-2400. (c) Nyquist plots derived from EIS measurements of $CeO_2$-$NiSe_2$-500, $CeO_2$-$NiSe_2$-1200, $CeO_2$-$NiSe_2$-2400.

**Figure S15.** (a) Diagram of the initial structure of $Ni(OH)_2$ and the intermediate state of the OER with adsorbed *OH, *O, *OOH. (b) Diagram of the initial structure of $Ni(OH)_2$-$NiSe_2$ and the intermediate state of the OER with adsorbed *OH, *O, *OOH.

**Figure S16.** (a, b) Differential charge densities of $Ni(OH)_2$ and $Ni(OH)_2$-$NiSe_2$ structures. (c, d) Density of states of $Ni(OH)_2$ and $Ni(OH)_2$-NiSe structures.

**Figure S17.** HER free-energy evolutions of the $Ni(OH)_2$, $Ni(OH)_2$-$NiSe_2$ and $CeO_2$-$NiSe_2$ structures.

## 3. Supplementary Tables

**Table S1.** The detailed determination of cerium, nickel, selenium and oxygen elements calculated by means of ICP-MS and EA methods for $CeO_2$-$NiSe_2$.

**Table S2.** Comparison of as-obtained hybrids of OER performance at large current densities.

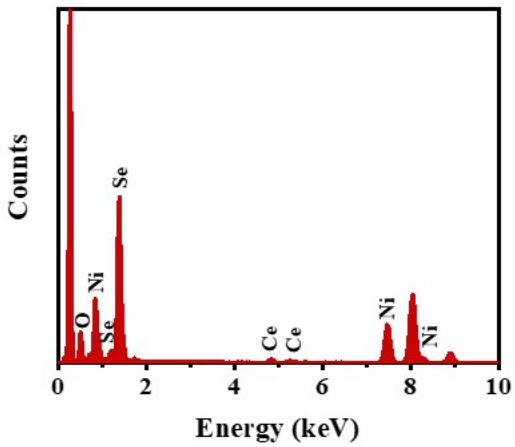


**Figure S1.** EDX plot of $CeO_2$-$NiSe_2$.

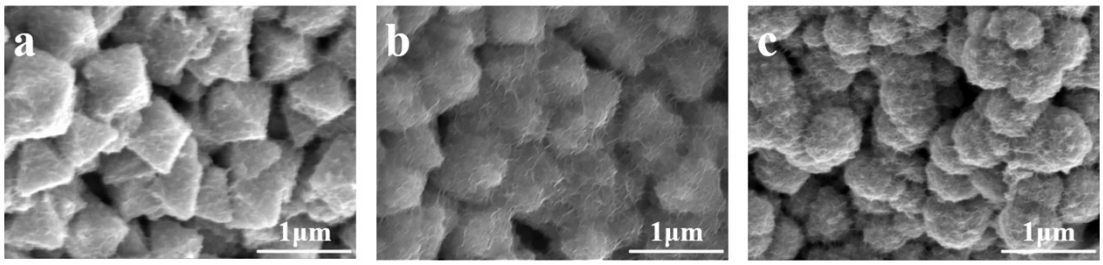


**Figure S2.** SEM images of (a) $CeO_2$-$NiSe_2$-500, (b) $CeO_2$-$NiSe_2$-1200, (c) $CeO_2$-$NiSe_2$-2400.

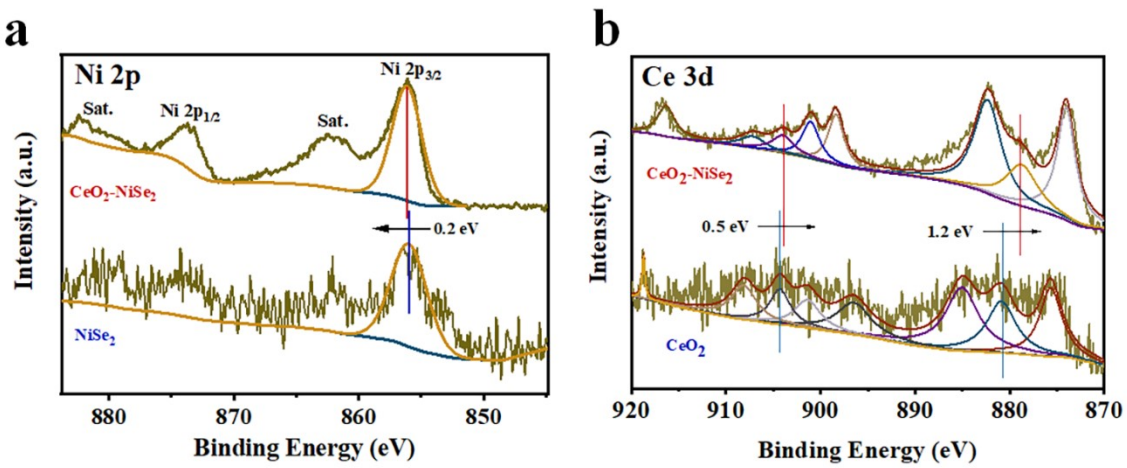


**Figure S3.** (a), (b) Ni 2p and Ce 3d XPS spectrum of $CeO_2$-$NiSe_2$ and $NiSe_2$.

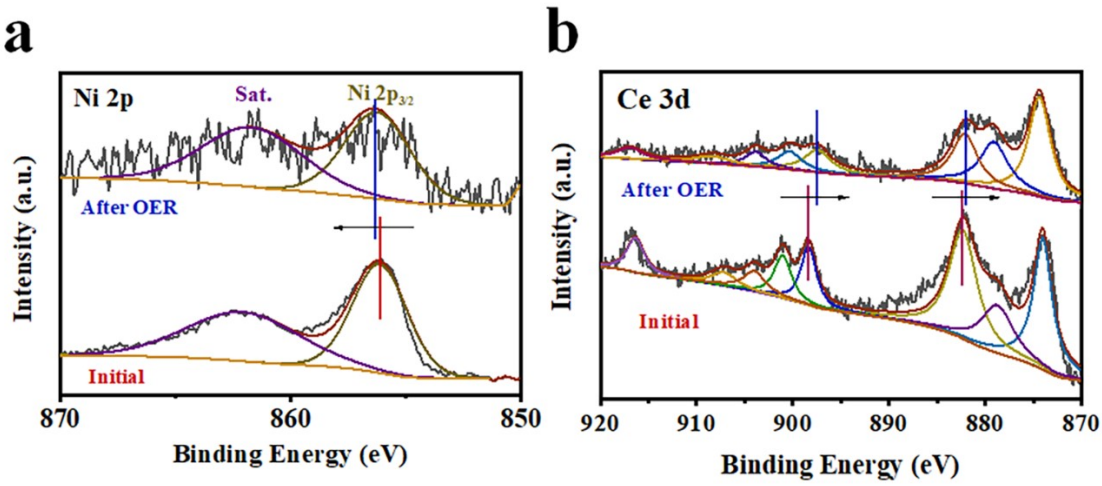


**Figure S4.** XPS spectrum of (a) $CeO_2$-$NiSe_2$ before OER stability test and (b) $CeO_2$-$NiSe_2$ after OER stability test.

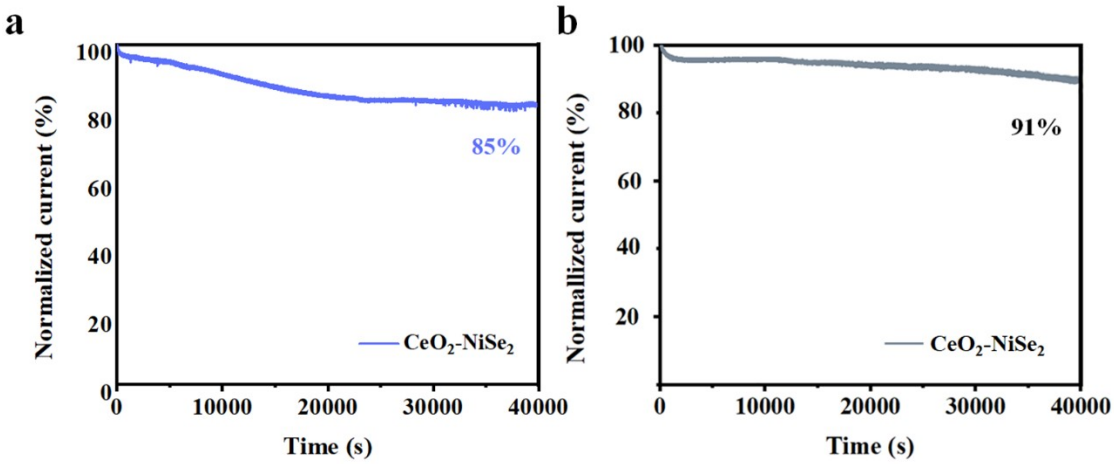


**Figure S5.** Chronopotentiometry measurements on the long-term stability of the $CeO_2$-$NiSe_2$ during (a) OER and (b) HER electrolysis at a current density of 50 mA $cm^{-2}$ (percentage of voltage retained vs operation time).

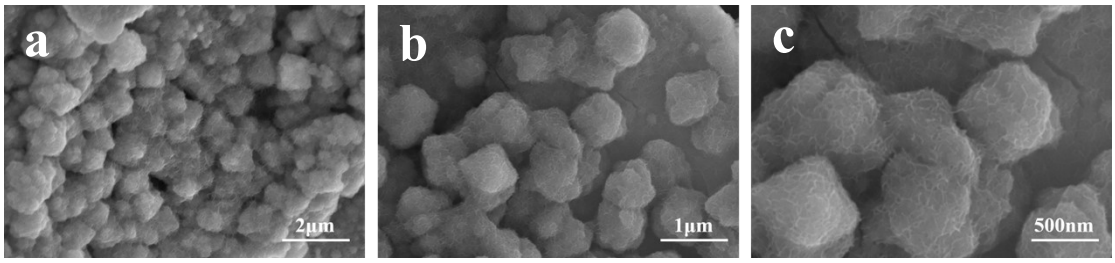


**Figure S6.** (a)-(c) SEM images of $CeO_2$-$NiSe_2$ after OER stability test.

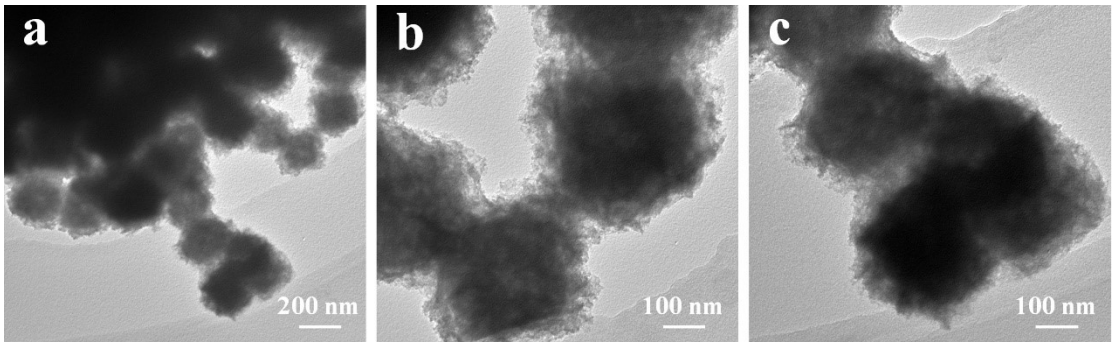


**Figure S7**. (a)-(c) TEM images of $CeO_2$-$NiSe_2$ after OER stability test.

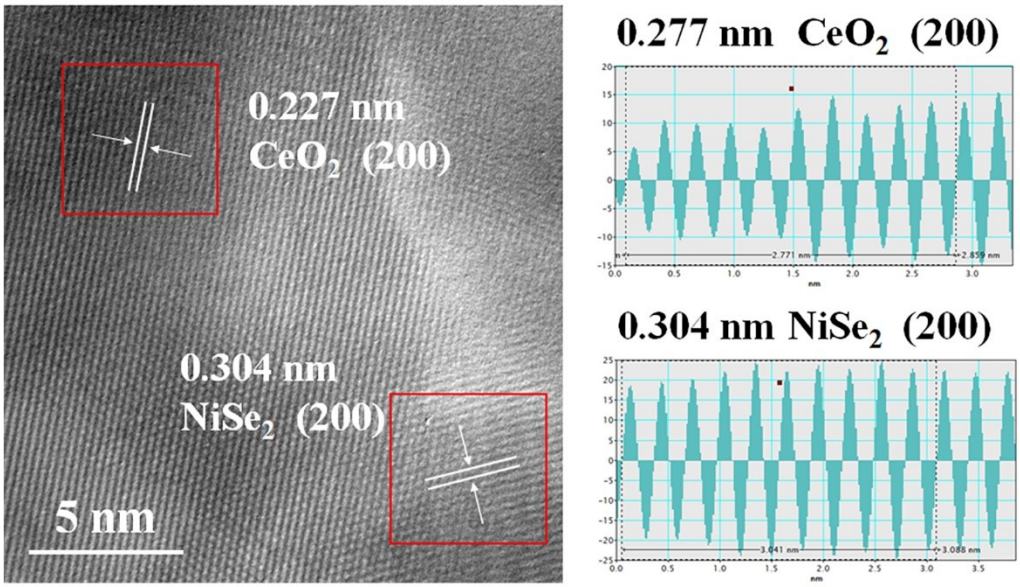


**Figure S8.** HRTEM images of $CeO_2$-$NiSe_2$ after OER stability test.

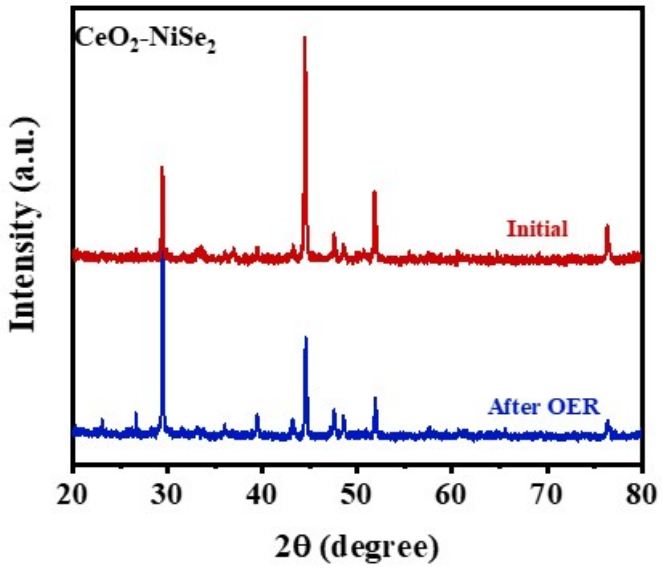


**Figure S9.** XRD pattern of $CeO_2$-$NiSe_2$ before and after OER stability test.

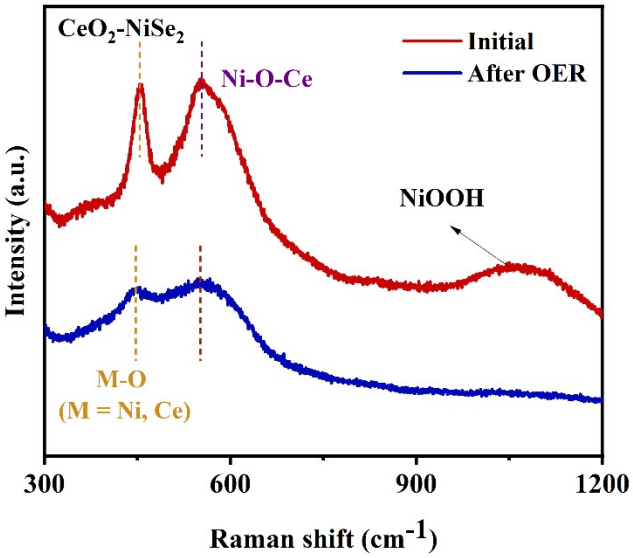


**Figure S10.** Raman spectrum of $CeO_2$-$NiSe_2$ before and after OER stability test.

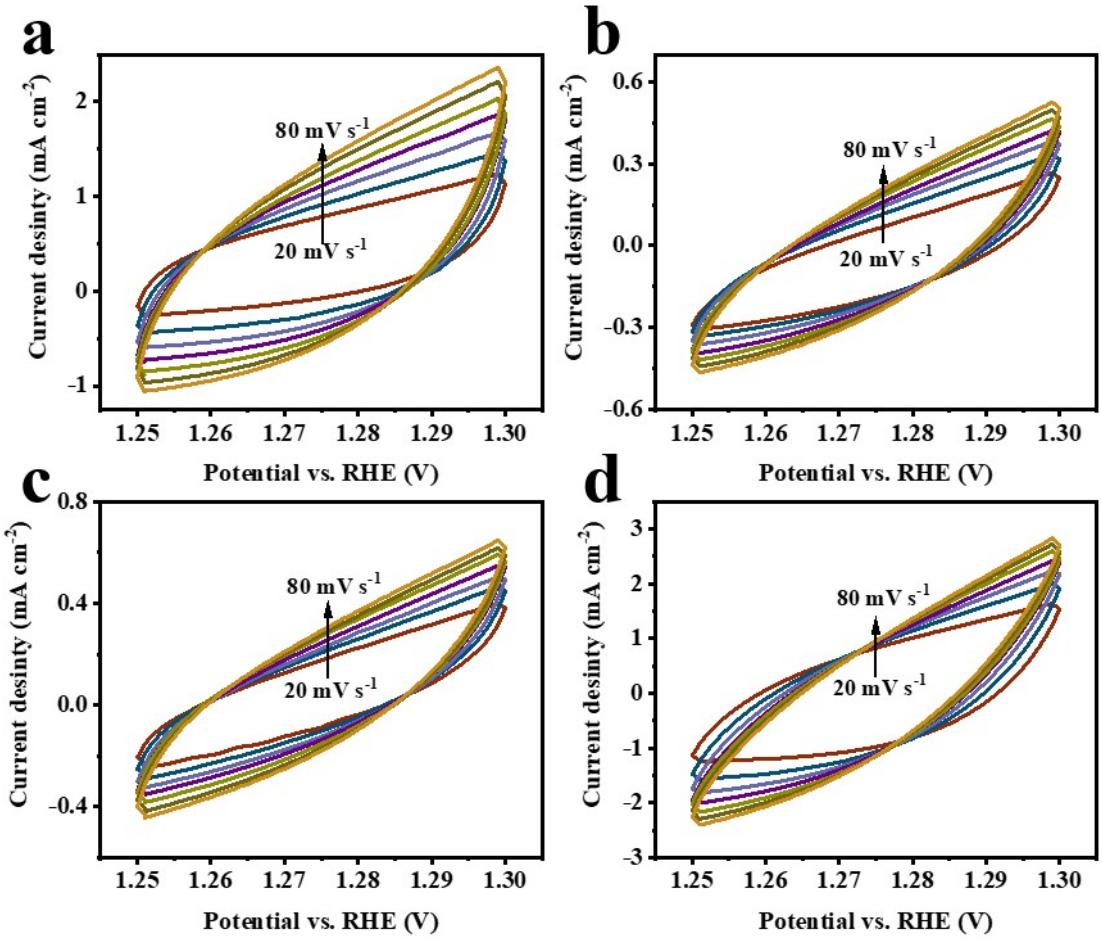


**Figure S11.** CVs of OER measurements in 1 M KOH at scan rates from 20 to 80 mV $s^{-1}$ for (a) $CeO_2$-$NiSe_2$, (b) $Ni(OH)_2$, (c) $NiSe_2$ and (d) $CeO_2$.

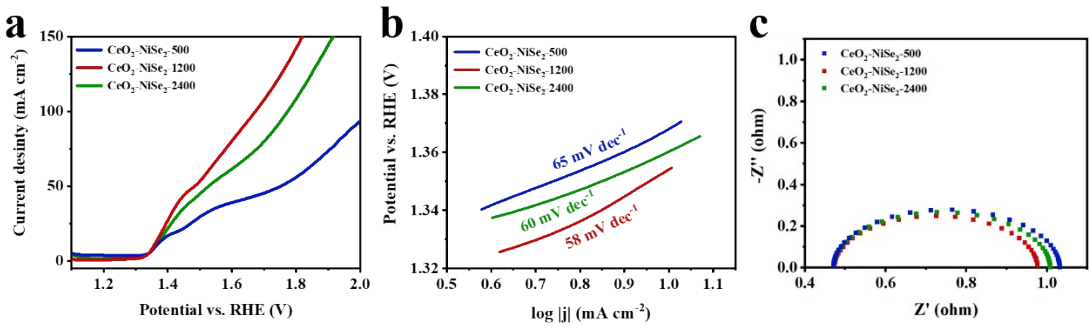


**Figure S12.** OER performance of $CeO_2$-$NiSe_2$ at different deposition time. (a) LSV curves of $CeO_2$-$NiSe_2$-500, $CeO_2$-$NiSe_2$-1200, $CeO_2$-$NiSe_2$-2400. (b) Tafel plots of $CeO_2$-$NiSe_2$-500, $CeO_2$-$NiSe_2$-1200, $CeO_2$-$NiSe_2$-2400. (c) Nyquist plots derived from EIS measurements of $CeO_2$-$NiSe_2$-500, $CeO_2$-$NiSe_2$-1200, $CeO_2$-$NiSe_2$-2400.

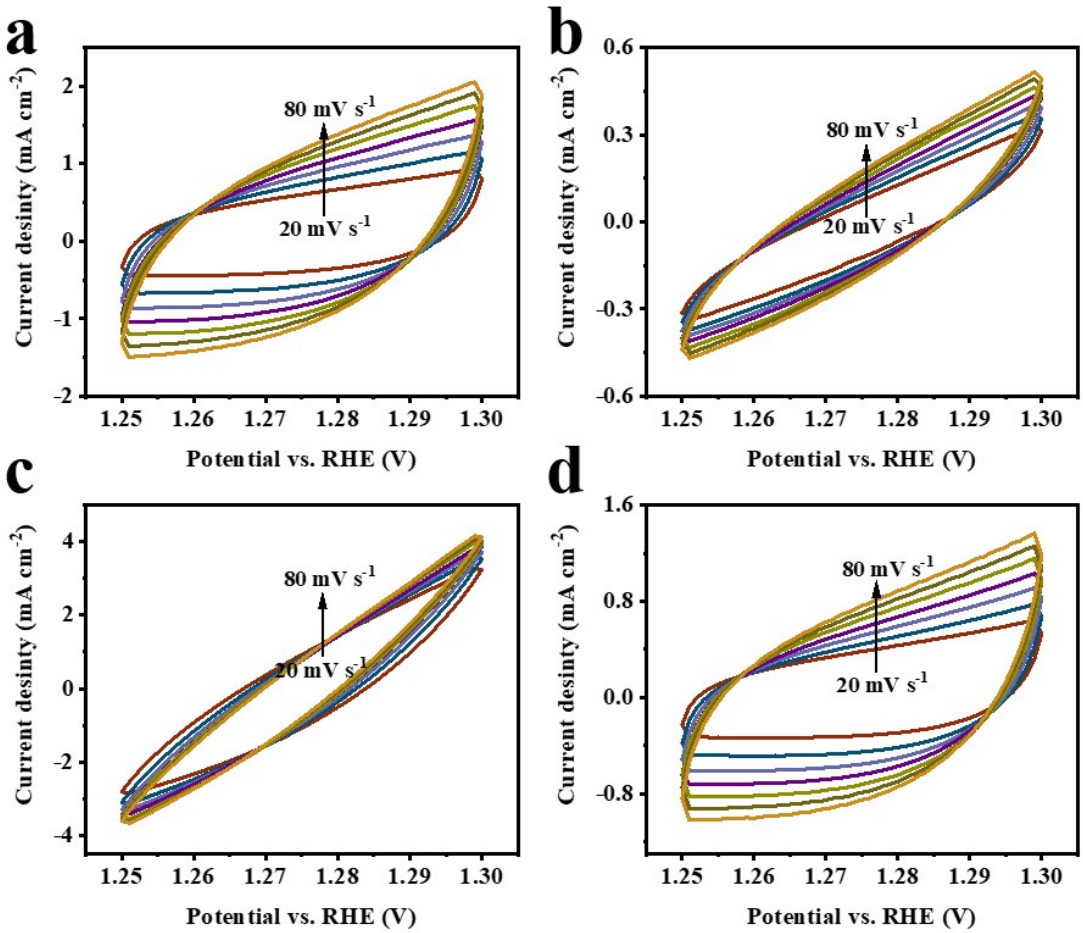


**Figure S13.** CVs of HER measurements in 1 M KOH at scan rates from 20 to 80 mV $s^{-1}$ for (a) $CeO_2$-$NiSe_2$, (b) $Ni(OH)_2$, (c) $NiSe_2$ and (d) $CeO_2$.

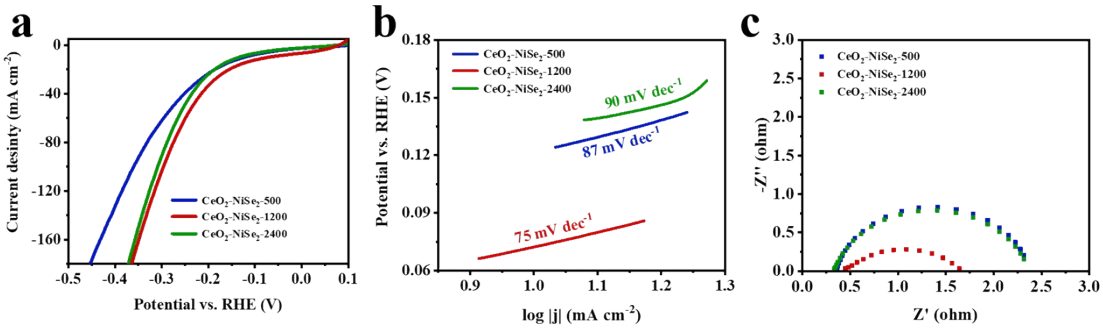


**Figure S14.** HER performance of $CeO_2$-$NiSe_2$ at different deposition time. (a) LSV curves of $CeO_2$-$NiSe_2$-500, $CeO_2$-$NiSe_2$-1200, $CeO_2$-$NiSe_2$-2400. (b) Tafel plots of $CeO_2$-$NiSe_2$-500, $CeO_2$-$NiSe_2$-1200, $CeO_2$-$NiSe_2$-2400. (c) Nyquist plots derived from EIS measurements of $CeO_2$-$NiSe_2$-500, $CeO_2$-$NiSe_2$-1200, $CeO_2$-$NiSe_2$-2400.

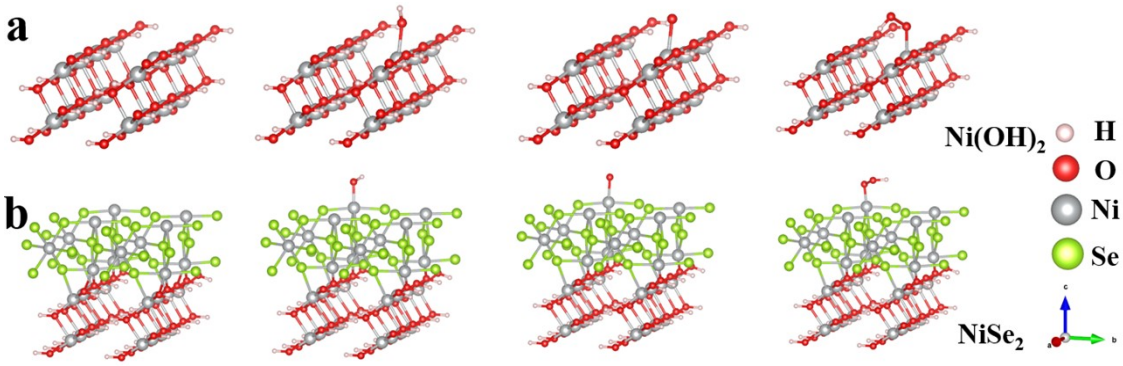


**Figure S15.** (a) Diagram of the initial structure of $Ni(OH)_2$ and the intermediate state of the OER with adsorbed *OH, *O, *OOH. (b) Diagram of the initial structure of $Ni(OH)_2$-$NiSe_2$ and the intermediate state of the OER with adsorbed *OH, *O, *OOH.

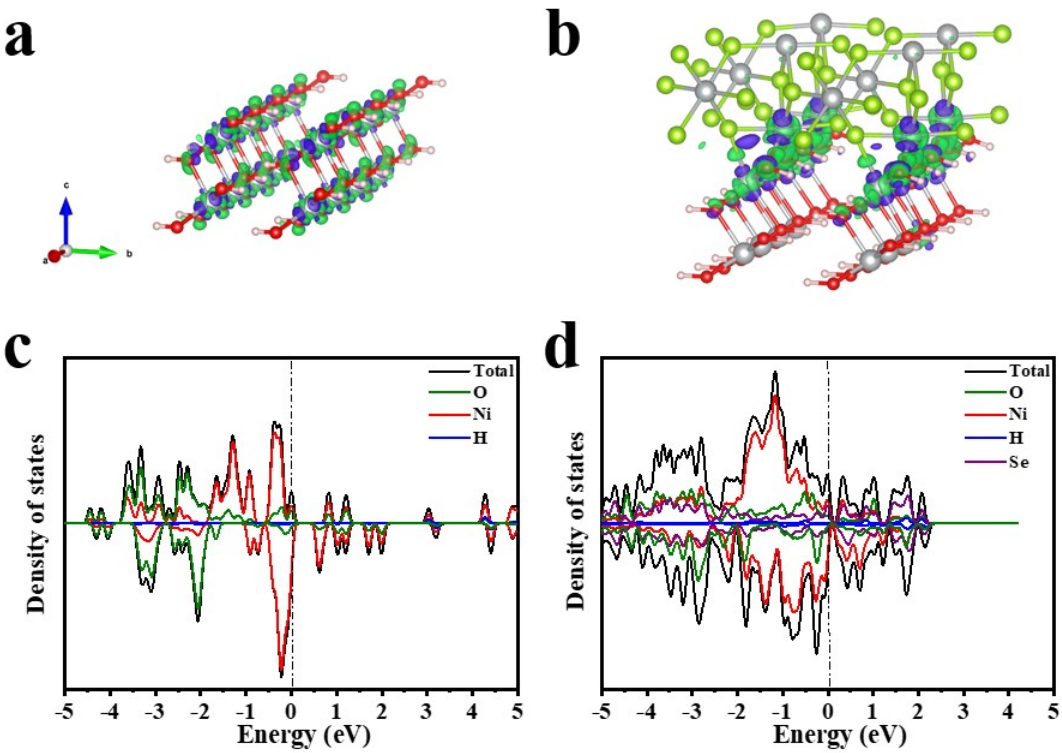


**Figure S16.** (a, b) Differential charge densities of $Ni(OH)_2$ and $Ni(OH)_2$-$NiSe_2$ structures. (c, d) Density of states of $Ni(OH)_2$ and $Ni(OH)_2$-$NiSe_2$ structures.

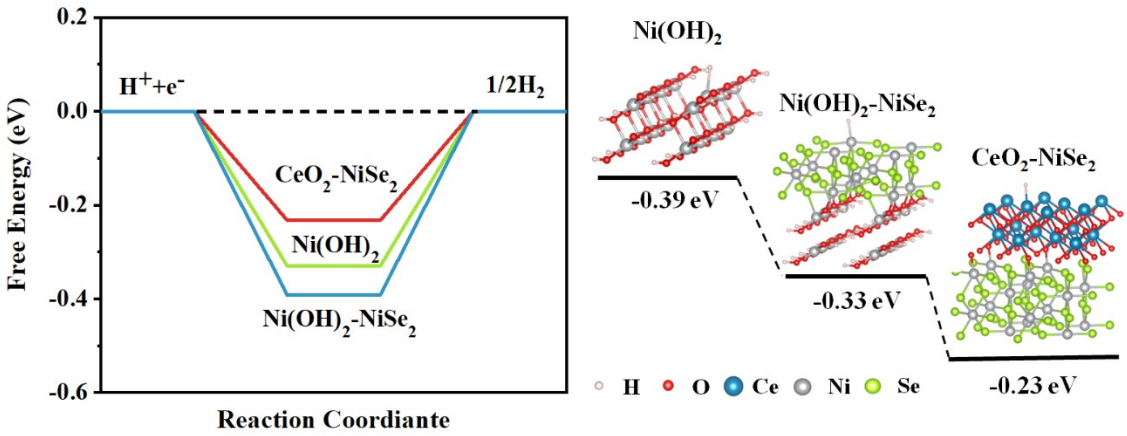


**Figure S17.** HER free-energy evolutions of the $Ni(OH)_2$, $Ni(OH)_2$-$NiSe_2$ and $CeO_2$-$NiSe_2$ structures.

**Table S1.** The detailed determination of cerium, nickel, selenium and oxygen elements calculated by means of ICP-MS and EA methods for $CeO_2$-$NiSe_2$.

| Methods | Sample weight (mg) | Ce (g/kg) | Ni (g/kg) | Se (g/kg) | O (%) |
|---|---|---|---|---|---|
| ICP-MS | 0.0134 | 89.50 | 202.73 | 493.15 | - |
| EA | 1.25 | - | - | - | 21.46 |

**Table S2**. Comparison of as-obtained hybrids of OER performance at large current densities.

| **Catalysts** | **Overpotential at 50 mA $cm^{-2}$ (mV)** | **Overpotential at 100 mA $cm^{-2}$ (mV)** |
|---|---|---|
| $CeO_2$-$NiSe_2$ | 250 | 442 |
| $NiSe_2$ | 400 | 547 |
| $CeO_2$ | 480 | 637 |
| $RuO_2$/NF | 380 | 522 |
| $Ni(OH)_2$ | - | - |

## References


1. G. Kresse and J. Furthmüller, Efficiency of Ab-Initio Total Energy Calculations for Metals and Semiconductors Using a Plane-Wave Basis Set, *Comput. Mater. Sci*., 1996, **6**, 15−50.

2. G. Kresse and J. Furthmüller, Efficient Iterative Schemes for Ab Initio Total-Energy Calculations Using a Plane-Wave Basis Set, *Phys. Rev. B*, 1996, **54**, 11169−11186.

3. J. P. Perdew, K. Burke and M. Ernzerhof, Generalized Gradient Approximation Made Simple, *Phys. Rev. Lett*., 1996, **77**, 3865−3868.

4. G. Kresse, D. Joubert, From Ultrasoft Pseudopotentials to the Projector Augmented-Wave Method, *Phys. Rev. B*, 1999, **59**, 1758-1775.

5. P. E Blöchl, Projector Augmented-Wave Method, *Phys. Rev. B*, 1994, **50** 17953−17979.